

# Electron-Doping Mottronics in Strongly Correlated Perovskite

Jikun Chen,\* Wei Mao, Lei Gao, Fengbo Yan, Takeaki Yajima, Nuofu Chen,\* Zhizhong Chen, Hongliang Dong, Binghui Ge, Peng Zhang, Xingzhong Cao,\* Markus Wilde, Yong Jiang,\* Takayuki Terai, and Jian Shi\*

HPSTAR  
882-2019

The discovery of hydrogen-induced electron localization and highly insulating states in d-band electron correlated perovskites has opened a new paradigm for exploring novel electronic phases of condensed matters and applications in emerging field-controlled electronic devices (e.g., Mottronics). Although a significant understanding of doping-tuned transport properties of single crystalline correlated materials exists, it has remained unclear how doping-controlled transport properties behave in the presence of planar defects. The discovery of an unexpected high-concentration doping effect in defective regions is reported for correlated nickelates. It enables electronic conductance by tuning the Fermi-level in Mott–Hubbard band and shaping the lower Hubbard band state into a partially filled configuration. Interface engineering and grain boundary designs are performed for  $H_x\text{SmNiO}_3/\text{SrRuO}_3$  heterostructures, and a Mottronic device is achieved. The interfacial aggregation of hydrogen is controlled and quantified to establish its correlation with the electrical transport properties. The chemical bonding between the incorporated hydrogen with defective  $\text{SmNiO}_3$  is further analyzed by the positron annihilation spectroscopy. The present work unveils new materials physics in correlated materials and suggests novel doping strategies for developing Mottronic and iontronic devices via hydrogen-doping-controlled orbital occupancy in perovskite heterostructures.

Hydrogen (proton) induced switchable multiphase transformations in d-band electron-correlated materials recently opened a new field for exploring merging multifunctional proton-gated electronic devices,<sup>[1]</sup> synaptic plasticity,<sup>[2,3]</sup> sensors,<sup>[4]</sup> and novel energy conversion devices.<sup>[5]</sup> Compared to other dopant elements, hydrogen is small in radius and has high ionic mobility.<sup>[1,4–6]</sup> Therefore, the proton distribution is highly adjustable via external electric fields, and the respective tuning of the physical properties of materials is feasible. This is, in particular, the case for the hydrogen-induced sharp transitions in electron orbital configurations and the magnetoelectric/spintronic states for d-band electron-correlated materials, such as  $\text{SmNiO}_3$ ,<sup>[1–5]</sup>  $\text{SrCoO}_{3-\delta}$ ,<sup>[6]</sup> and  $\text{VO}_2$ .<sup>[7]</sup> As a typical example, the hydrogenation of the perovskite-structured  $\text{SmNiO}_3$  d-band electron-correlated system results in an abrupt electronic transition of the  $e_g$  orbital from the electron-itinerant  $\text{Ni}^{3+}t_{2g}^6e_g^1$  state to the electron-localized  $\text{Ni}^{2+}t_{2g}^6e_g^2$

Prof. J. Chen, Prof. L. Gao, F. Yan, Prof. Y. Jiang  
Beijing Advanced Innovation Center for Materials Genome Engineering  
School of Materials Science and Engineering  
University of Science and Technology Beijing  
Beijing 100083, China  
E-mail: jikunchen@ustb.edu.cn; yjiang@ustb.edu.cn

Dr. W. Mao, Dr. T. Yajima, Prof. T. Terai  
School of Engineering  
The University of Tokyo  
2-11-16 Yayoi, Bunkyo-ku, Tokyo 113-0032, Japan

Prof. N. Chen  
School of Renewable Energy  
North China Electric Power University  
Beijing 102206, China  
E-mail: nfchen@ncepu.edu.cn

Z. Chen, Prof. J. Shi  
Department of Materials Science and Engineering  
Rensselaer Polytechnic Institute  
Troy, NY 12180, USA  
E-mail: shij4@rpi.edu

Prof. H. Dong  
Center for High Pressure Science and Technology Advanced Research  
Shanghai 201203, China

Prof. B. Ge  
Institute of Physical Science and Information Technology  
Anhui University  
Heifei 230601, Anhui, China

Dr. P. Zhang, Prof. X. Cao  
Institute of High Energy Physics  
Chinese Academy of Sciences  
Beijing 100049, China  
E-mail: caoxzh@ihep.ac.cn

Prof. M. Wilde  
Institute of Industrial Science  
The University of Tokyo  
4-6-1 Komaba, Meguro-ku, Tokyo 153-8505, Japan

 The ORCID identification number(s) for the author(s) of this article can be found under <https://doi.org/10.1002/adma.201905060>.

DOI: 10.1002/adma.201905060

state.<sup>[1–5]</sup> This was reported to sharply increase the electronic resistivity by several orders of magnitude,<sup>[1,2,4,5]</sup> while hydrogenated SmNiO<sub>3</sub> is expected to be proton conductive.<sup>[4]</sup> Although a considerable understanding of the transport properties has been established for single crystalline H<sub>x</sub>SmNiO<sub>3</sub> (Ni<sup>2+</sup>t<sub>2g</sub><sup>6</sup>e<sub>g</sub><sup>2</sup>) and other proton-doped correlated materials, it remains entirely unclear how doping-controlled transport properties behave in the presence of interfaces and microstructure. In conventional materials, it is known that hydrogen (proton) is often thermodynamically favored to be aggregated at interfaces.<sup>[8–10]</sup> Thus, through the possibility of selective hydrogen-doping in defective regions within strongly correlated materials, defect-controlled hydrogen doping and the associated tuning of transport properties may open novel avenues for designing proton-gated electronic devices.

In this work, we report the presence of an unexpected hydrogen doping effect at high concentration in hydrogen aggregation regions such as grain boundaries and incoherent interfaces (i.e., film and substrate lattices are not in registry) within SmNiO<sub>3</sub>. Such hydrogen doping overcompensates the previously reported hydrogenation-induced electron localization and results in electrical conductance by elevating the Fermi-level into the Hubbard band via converting the electron configuration from t<sub>2g</sub><sup>6</sup>e<sub>g</sub><sup>2</sup> to t<sub>2g</sub><sup>6</sup>e<sub>g</sub><sup>3</sup>. We performed interface engineering and grain boundary designs for H<sub>x</sub>SmNiO<sub>3</sub>/SrRuO<sub>3</sub> heterostructures. Apart from realizing a highly insulating state by triggering electron localization in the bulk region, the H<sub>x</sub>SmNiO<sub>3</sub>/SrRuO<sub>3</sub> heterostructures can further achieve diode behavior, when high-concentration hydrogen is found through the entire grain boundary region of the film via electrical field-assisted migration. Guided by hydrogen depth profiling via resonant <sup>1</sup>H(<sup>15</sup>N,α)<sup>12</sup>C nuclear reaction analysis (NRA), we controlled and quantified the interfacial aggregation of hydrogen to understand its correlation with the electrical transport properties. Concomitant with the hydrogen interfacial aggregation, we demonstrate a switchable electronic diode based on electron-correlated polycrystalline H<sub>x</sub>SmNiO<sub>3</sub>/SrRuO<sub>3</sub> heterostructures.

In previous reports, the hydrogenation is (first, i.e., at low H concentrations) expected to trigger a sharp electronic phase transition of the SmNiO<sub>3</sub> from the electron itinerant t<sub>2g</sub><sup>6</sup>e<sub>g</sub><sup>1</sup> state to the electron localized t<sub>2g</sub><sup>6</sup>e<sub>g</sub><sup>2</sup> state<sup>[1,2,4,5]</sup> to open a wider bandgap (the extra electrons fill into the p–d hybridized orbits with strong p character since perovskite nickelates carry strong covalency; whether this is a negative or positive transfer insulator<sup>[11,12]</sup> does not change the characteristic proposed here). Now, what happens if the SmNiO<sub>3</sub> is doped with higher concentration of hydrogen? It should be noted that hydrogen (proton) tends to aggregate at the incoherent material interfaces, lattice defects, and grain boundaries.<sup>[8]</sup> Combining such a hydrogen doping with electronic field regulation in hydrogenated Pt/H<sub>x</sub>SmNiO<sub>3</sub>/SrRuO<sub>3</sub> polycrystalline heterostructures should thus make it possible to realize electronic diode behavior. Based on our hypothesis, the overhydrogenation is expected to result in higher electron conductivity for grain boundaries within H<sub>x</sub>SmNiO<sub>3</sub>.<sup>[1,2,4,5]</sup> The grain boundaries within the heterostructure are hydrogen aggregation locations, and can behave as migration channels for protons when a sufficiently large negative bias voltage (V<sub>Ext</sub>) is applied to the platinum (Pt) electrode. The electric field-assisted migration of hydrogen would then heavily

dope the grain boundary that abruptly reduces the cross-plane resistance by triggering more t<sub>2g</sub><sup>6</sup>e<sub>g</sub><sup>3</sup> configuration occupancy. This is thus a low-R (“on”) state. When positive bias is applied, protons will be depleted from the grain boundary making it lose its t<sub>2g</sub><sup>6</sup>e<sub>g</sub><sup>3</sup> configuration and instead accumulate at the heterojunction interface, which then takes a t<sub>2g</sub><sup>6</sup>e<sub>g</sub><sup>2</sup> configuration. In this condition, the overall resistance is high, so this is a high-R (“off”) state.

To realize the above concept, a deposition strategy of polycrystalline ReNiO<sub>3</sub> films on the bottom electrode layer without involving prior high-pressure annealing is required. The key point to deposit rare-earth nickelates is thus to reduce the nucleation barrier (ΔG),<sup>[13]</sup> as previously achieved via high pressure oxygen annealing<sup>[13–16]</sup> or co-lattice epitaxy of ReNiO<sub>3</sub> on single crystal perovskite substrates as templates.<sup>[16–19]</sup> In contrast to these previous reports, herein, we have successfully (Figure 3a) grown polycrystalline SmNiO<sub>3</sub> and NdNiO<sub>3</sub> on a SrRuO<sub>3</sub>-buffered silicon substrate by pulsed laser deposition (PLD), without involving any high pressure annealing procedures. The SrRuO<sub>3</sub> buffer layer exhibits a similar crystal structure and lattice constant as ReNiO<sub>3</sub>, and hence serves as a lattice template for heterogeneous nucleation of SmNiO<sub>3</sub> at reduced nucleation barrier. This is qualitatively demonstrated by the results from density functional theory (DFT) calculations shown in Figure 1a, while further details are demonstrated in Section S1 in the Supporting Information. In this simulation, the analyses were carried out at SmNiO<sub>3</sub>(121)/SrRuO<sub>3</sub>(121) interface, as the lattice in the plane of SmNiO<sub>3</sub>(121) matches well to the one of SrRuO<sub>3</sub>(121). The resultant strong chemical interaction indicated by the charge transfer isosurfaces at the interface can effectively reduce the free energy of the system, which acts a driving force for the epitaxial growth of SmNiO<sub>3</sub>.

Following this strategy, we grew polycrystalline SmNiO<sub>3</sub>/SrRuO<sub>3</sub>/Si heterostructures by PLD. As demonstrated by their X-ray diffraction (XRD) patterns in Figure 1b, as-deposited SmNiO<sub>3</sub> on the SrRuO<sub>3</sub> buffer layer exhibits a polycrystalline structure with similar orientations compared to as-deposited SrRuO<sub>3</sub>. In contrast, the desired phase and structure of SmNiO<sub>3</sub> was not achieved via direct deposition on the Si substrate without the presence of the SrRuO<sub>3</sub> buffer layer. The surfaces of the as-deposited SrRuO<sub>3</sub> buffer layer and the SmNiO<sub>3</sub> films deposited subsequently are flat with a roughness of only a few nanometers, as indicated by their atomic force microscopy images in Figure S1a in the Supporting Information. As the cross-section transmission electron microscopy (TEM) images and energy-dispersive X-ray spectroscopy (EDS) depth profile show in Figure 1c, the as-grown SrRuO<sub>3</sub> and SmNiO<sub>3</sub> films exhibit polycrystalline structures with grain sizes of several tens of nanometers (Figure S1b,c in the Supporting Information shows more TEM and EDS results). The same approach was used to successfully fabricate polycrystalline NdNiO<sub>3</sub> films on silicon or quartz substrates buffered with SrRuO<sub>3</sub>, as further demonstrated in Figure S1d in the Supporting Information. For further comparisons, we also deposited quasi-single crystalline heterostructures of SmNiO<sub>3</sub>/SrRuO<sub>3</sub>/SrTiO<sub>3</sub>(001) and Pt/SmNiO<sub>3</sub>/SrRuO<sub>3</sub>/LaAlO<sub>3</sub>(001). Their XRD patterns are shown in Figure S1e in the Supporting Information, while their film–substrate interfacial coherency is demonstrated by reciprocal space mapping (RSM) as shown in Figure S1f,g in the Supporting Information.

To hydrogenate the  $\text{SmNiO}_3/\text{SrRuO}_3$  heterostructures, patterned Pt top electrodes were deposited onto the surface of  $\text{SmNiO}_3$ , and afterward the heterostructures were annealed in 1%  $\text{H}_2/\text{He}$  gas mixture. We directly and quantitatively probed the depth distribution of the  $^1\text{H}$  composition within various  $\text{Pt}/\text{H}_x\text{SmNiO}_3/\text{SrRuO}_3$  heterostructures based on  $^1\text{H}(^{15}\text{N}, \alpha\gamma)^{12}\text{C}$  resonant NRA<sup>[20]</sup> (see schematic illustration in Figure S2 in the Supporting Information). Figure 1d shows the  $^1\text{H}$  depth profiles of the polycrystalline  $\text{Pt}/\text{SmNiO}_3/\text{SrRuO}_3/\text{Si}$  heterostructures after various periods of hydrogenation. The  $^1\text{H}$  distributes broadly from the  $\text{SrRuO}_3/\text{Si}$  interface, across the  $\text{SrRuO}_3$  ( $\approx 20$  nm), and further into the layer of  $\text{SmNiO}_3$  by  $\approx 120$  nm. This is in contrast to the situation for the single crystalline heterostructures grown on  $\text{SrTiO}_3(001)$  and  $\text{LaAlO}_3(001)$  substrates as shown in Figure 1e, in which cases higher concentration of  $^1\text{H}$  distributes within a narrower region around the incoherent interfaces. Without grain boundaries, it is difficult for hydrogen to diffuse out of the interfacial region.

Figure 2 shows the current–voltage ( $I$ – $V$ ) characteristics of the hydrogenated  $\text{Pt}/\text{SmNiO}_3/\text{SrRuO}_3/\text{substrate}$  heterostructures, while their representative current density to electric field ( $J$ – $E$ ) characteristics are demonstrated in Figure S3 in the Supporting Information. In contrast to the previous understanding that hydrogenating  $\text{Pt}/\text{SmNiO}_3$  significantly elevates the electronic resistivity,<sup>[1–5]</sup> herein, an electronic diode behavior is observed for the hydrogenated polycrystalline  $\text{Pt}/\text{SmNiO}_3/\text{SrRuO}_3/\text{Si}$ . As demonstrated in Figure 2a, when imparting a monodirectional external bias ( $V_{\text{Ext}}$ ) larger than  $\approx 5$  V pointing from the  $\text{SrRuO}_3$  toward the Pt electrode, an abrupt reduction of the resistance by a factor of  $\approx 50$  was observed. In contrast, similar reductions in electronic resistance are not achieved when loading  $V_{\text{Ext}}$  in the opposite direction or at smaller magnitude. It is worth noticing that the  $V_{\text{Ext}}$ -triggered reduction in resistivity is monodirectional (like in an electronic diode). Such behavior differs clearly from the varistor behavior in oxides such as doped  $\text{ZnO}$  or  $\text{TiO}_2$ ,<sup>[21,22]</sup> or from the soft breakdown of oxide gates,<sup>[23–25]</sup> and should be attributed mainly to  $\text{SmNiO}_3$

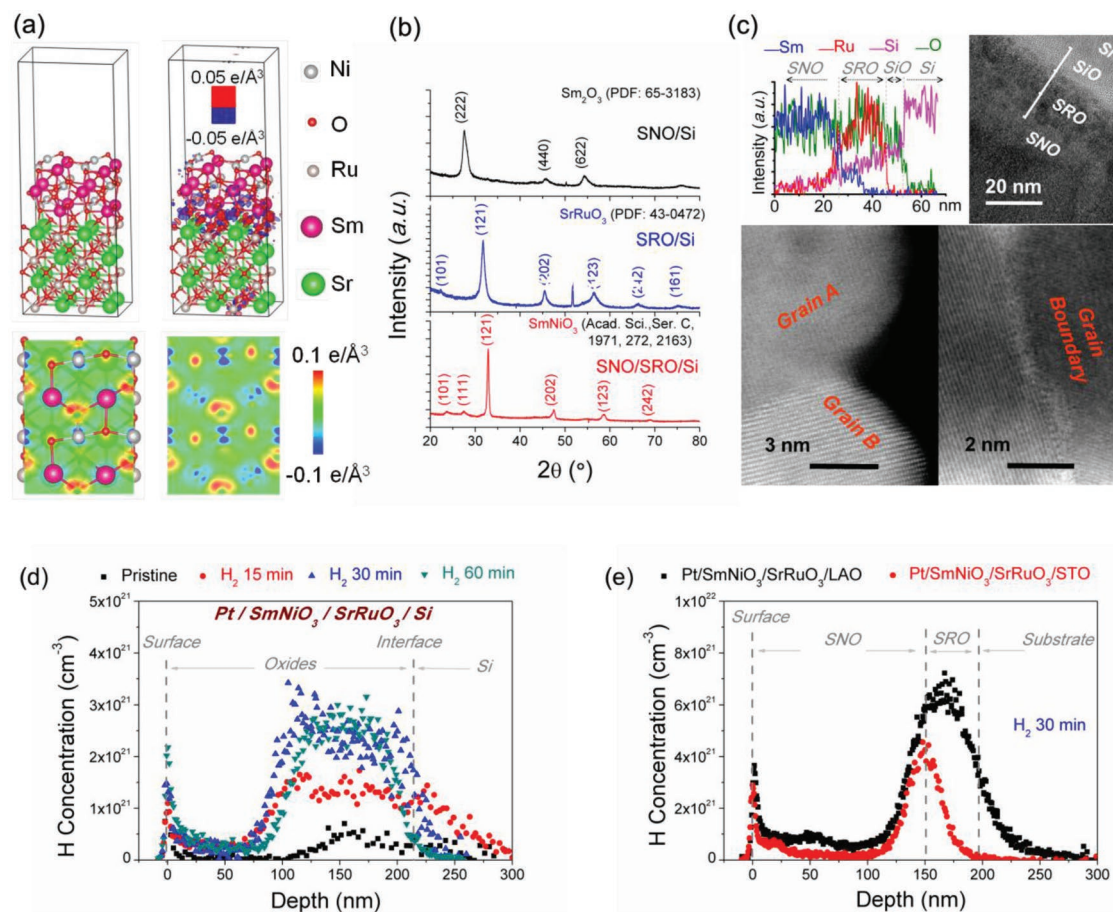


**Figure 1.** Establishing the model heterostructures of nickelate ionic Mottronics. a) Density functional theory (DFT) calculations to qualitatively reveal driving force of  $\text{SmNiO}_3$  growing on  $\text{SrRuO}_3$ . Top-left: Relaxed structure of three layers of  $\text{SmNiO}_3(121)$  growing on  $\text{SrRuO}_3(121)$ . Top-right: Isosurfaces indicating strong chemical interaction at the interface of  $\text{SmNiO}_3(121)/\text{SrRuO}_3(121)$ . Down: Charge transfer distributions of  $\text{SmNiO}_3(121)/\text{SrRuO}_3(121)$  to illustrate the strong  $\text{Sr}-\text{O}$ ,  $\text{Sm}-\text{O}$ , and  $\text{Ni}-\text{O}$  bonds. b) X-ray diffraction patterns ( $2\theta$ -scan) of as-grown  $\text{SmNiO}_3/\text{Si}(001)$ ,  $\text{SrRuO}_3/\text{Si}(001)$ , and  $\text{SmNiO}_3/\text{SrRuO}_3/\text{Si}(001)$ . c) Interfacial morphology and energy-dispersive X-ray spectroscopy (EDS) of as-grown  $\text{SmNiO}_3/\text{SrRuO}_3/\text{Si}(001)$ ; the high resolution image shows the grain boundary morphology of polycrystalline  $\text{SmNiO}_3$ . d,e) Resonant nuclear reaction analysis (NRA) data for the hydrogenated d) polycrystalline  $\text{Pt}/\text{SmNiO}_3/\text{SrRuO}_3/\text{Si}$  heterostructures and e) quasi-single crystalline  $\text{Pt}/\text{SmNiO}_3/\text{SrRuO}_3/\text{LaAlO}_3$  and  $\text{Pt}/\text{SmNiO}_3/\text{SrRuO}_3/\text{SrTiO}_3$  heterostructures.

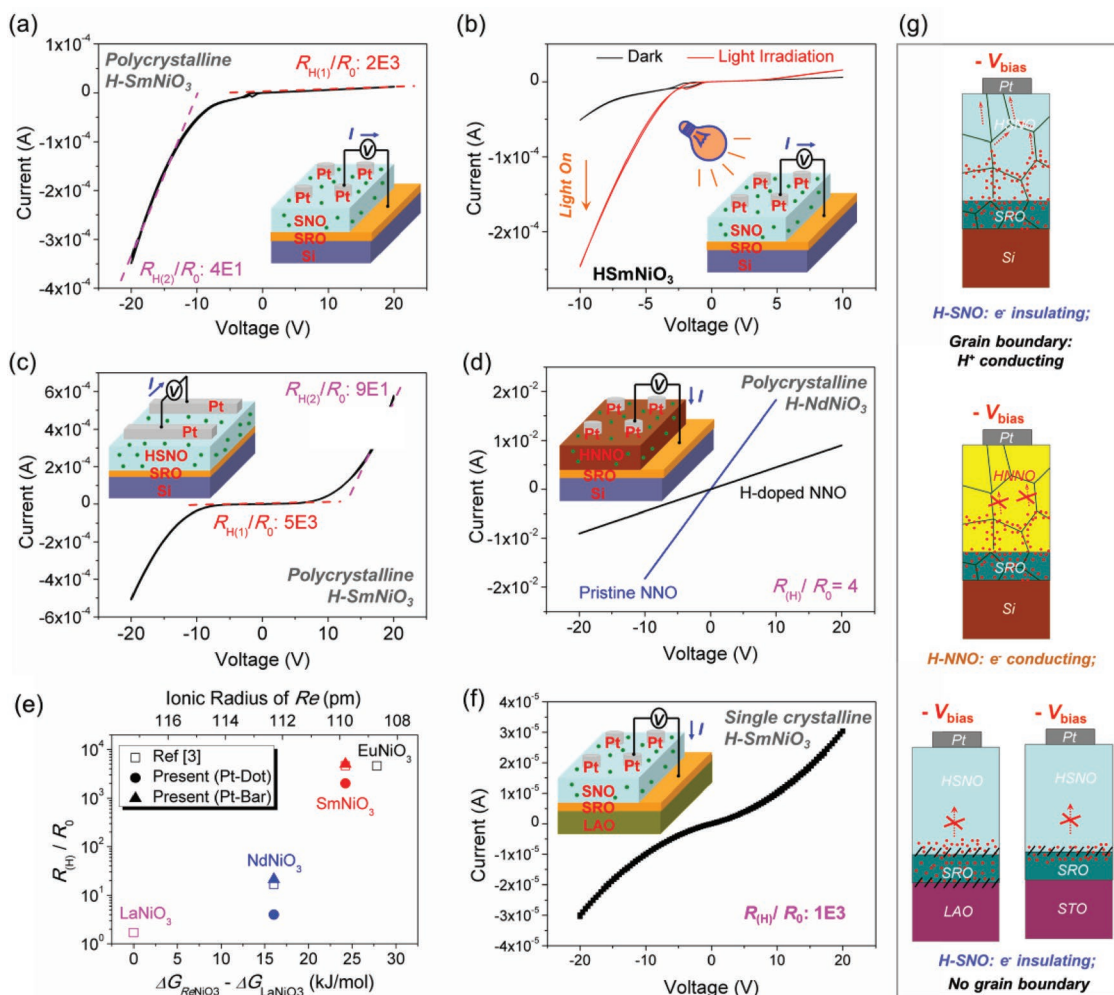


**Figure 2.** The transport characteristics for Pt/ $H_x$ ReNiO<sub>3</sub>/SrRuO<sub>3</sub> Mottronics. a,b) Volt–ampere ( $I$ - $V$ ) characteristics of the monodirectional Pt/ $H_x$ SmNiO<sub>3</sub>SrRuO<sub>3</sub>/Si polycrystalline heterostructures a) in dark and b) under illumination of photon from 400 to 700 nm. c) Bidirectional rectification behavior in Pt/ $H_x$ SmNiO<sub>3</sub>/SrRuO<sub>3</sub>/Si polycrystalline heterostructure when imparting the external voltage upon two Pt electrodes. d)  $I$ - $V$  characteristics of the hydrogenated Pt/NdNiO<sub>3</sub>/SrRuO<sub>3</sub>/Si exhibiting the similar structure to the one shown in (a). Each  $I$ - $V$  curve contains 100 points, while the time to measure each point last 50 ms. For Pt/ $H_x$ SmNiO<sub>3</sub> (polycrystalline)/SrRuO<sub>3</sub>/Si, two resistance,  $R_{H(1)}$  and  $R_{H(2)}$ , were obtained by section linear fitting that represent the high and low resistance state before and after the voltage-driven hydrogen doping, respectively. e) The ratio in the hydrogenation elevated resistivity for  $ReNiO_3$  ( $R_{H(1)}/R_0$ ) in this work and also those reported in ref. [3] plotted as a function of their relative formation energy ( $\Delta G_f$ ) compared to  $LaNiO_3$ . f)  $I$ - $V$  characteristics for quasi-single crystalline Pt/ $H_x$ SmNiO<sub>3</sub>/SrRuO<sub>3</sub>/LaAlO<sub>3</sub> with comparable structure compared to the one shown in (a). g) Schematic illustrations of the hydrogen (proton) distributions and transports under external bias for various heterostructures.

since no significant change in resistance was observed before and after the hydrogenation of SrRuO<sub>3</sub>. The monodirectional reduction in resistance is further amplified when irradiating the device with visible light, as shown in Figure 2b. The photon excitation may assist in overcoming the activation barrier required for the proton diffusion toward the Pt electrode and thereby facilitate the H migration process.

When imparting  $V_{Ext}$  upon two Pt electrodes, a voltage-driven bidirectional reduction in the resistivity was further achieved, and this is equivalent to the situation of inversely connecting two monodirectional Pt/ $H_x$ SmNiO<sub>3</sub>/SrRuO<sub>3</sub> heterostructures (e.g., Figure 2a) in parallel. This is further shown in Figure 2c, where an abrupt  $\approx 50$ -fold reduction of the resistance is observed when imparting a  $V_{Ext}$  exceeding  $\approx 10$  V upon two Pt electrodes along both directions. More such examples are

further shown in Figures S4 and S5 in the Supporting Information. It should be noted that when directly measuring the resistance on the surface of the hydrogenated SmNiO<sub>3</sub> film, the electric field induced reduction in resistivity is less significant (see Figure S5 in the Supporting Information).

In contrast to heterostructures based on SmNiO<sub>3</sub>, a similar diode behavior was not realized in the hydrogenated Pt/ $H_x$ NdNiO<sub>3</sub>/SrRuO<sub>3</sub>/Si polycrystalline heterostructure, although it exhibits similar hydrogen distribution (see its NRA results in Figure S6 in the Supporting Information). As demonstrated in Figure 2d, performing similar hydrogenation process upon the NdNiO<sub>3</sub>-based heterostructure results in much smaller elevations in the resistivity (below one order) compared to the ones based on SmNiO<sub>3</sub> (e.g., as shown in Figure 2a), while its  $I$ - $V$  behavior is linear rather than diode. It is worth

mentioning that at room temperature, the pristine NdNiO<sub>3</sub> is at metallic phase, while SmNiO<sub>3</sub> is at insulating (semiconducting) phase. More such confirmation examples are demonstrated in Figure S7 in the Supporting Information, e.g., for bidirectionally structured Pt (bar-shape)/NdNiO<sub>3</sub>/SrRuO<sub>3</sub>/Si. These results indicate that the applied  $V_{\text{Ext}}$  cannot be effectively loaded upon the hydrogenated NdNiO<sub>3</sub> owing to its much smaller resistivity compared to hydrogenated SmNiO<sub>3</sub>.<sup>[3]</sup> In Figure 2e, we further plot the ratio in the hydrogenation elevated resistivity for  $R_{\text{eNiO}_3}$  ( $R_{\text{H}}/R_0$ ), in this work and also those reported in ref. [3] as a function of their relative formation energy ( $\Delta G_{\text{f}}$ ) compared to LaNiO<sub>3</sub> calculated according to previous reports.<sup>[3,13]</sup> A larger  $R_{\text{H}}/R_0$  is observed for  $R_{\text{eNiO}_3}$  with more positive  $\Delta G_{\text{f}}$ , and this is in consistency to the reports by Chen et al.<sup>[3]</sup> Without effectively isolating the electron carriers similar to hydrogenated SmNiO<sub>3</sub>, the electric field regulations of protons within hydrogenated NdNiO<sub>3</sub> are ineffective.

Furthermore, the diode-like transport behavior was also not achieved in the hydrogenated quasi-single crystalline SmNiO<sub>3</sub>/SrRuO<sub>3</sub>-based heterostructures. As demonstrated in Figure 2f, a constant high resistance was observed when applying both positive and negative  $V_{\text{Ext}}$  to the hydrogenated Pt/SmNiO<sub>3</sub>/SrRuO<sub>3</sub>/LaAlO<sub>3</sub> (001) quasi-single crystalline heterostructure, while a similar  $I$ - $V$  character is observed for hydrogenated Pt/SmNiO<sub>3</sub>/SrRuO<sub>3</sub>/SrTiO<sub>3</sub> (001) as shown in Figure S8 in the Supporting Information. In terms of nonlinearity, it is worthy to note that these  $I$ - $V$  curves observed for quasi-single crystalline heterostructure drastically differ from the one observed for Pt/H<sub>x</sub>SmNiO<sub>3</sub>/SrRuO<sub>3</sub>/Si. The on/off ratio between the polycrystalline film (e.g., 28 on/off ratio for polycrystalline heterostructure showing in Figure 2a at  $\pm 20$  V) and quasi-single crystalline film (e.g., 0.98 on/off ratio for single crystalline heterostructure shown in Figure 2f at  $\pm 20$  V) differs by orders in magnitude. Therefore, although the intrinsic Schottky contact may also exist in polycrystalline Pt/H<sub>x</sub>SmNiO<sub>3</sub>/SrRuO<sub>3</sub>/Si, it should not be the dominate reason for their diode-like behavior. These results indicate the importance of grain boundaries to achieve the diode behavior and confirm our hypothesis that the proton is more likely to migrate via grain boundaries upon electrical field application, resulting in electronic conductance via more-heavily hydrogen doping. Additional results from the different temperature-dependent alternative current (AC) impedance spectra measured for these hydrogenated heterostructures (see Figures S9 and S10 in the Supporting Information) further confirm this understanding.

To further explore the correlation between the hydrogen concentration and the electrical conductance it induces, we sandwiched a thin layer of polycrystalline SmNiO<sub>3</sub> ( $\approx 20$  nm) between single crystalline SmNiO<sub>3</sub> and LaAlO<sub>3</sub>, as its cross-section morphology shows in Figure 3a. This structure is achieved by performing thermoshock to artificially destroy the interfacial coherency, and the Pt/SmNiO<sub>3</sub>/LaAlO<sub>3</sub> was hydrogenated in 1% H<sub>2</sub>/He for various durations ( $t$ ). Figure 3b demonstrates their hydrogen depth profiles across the interfacial region measured by NRA, while more detailed analysis is shown in Figure S11 in the Supporting Information. The profiles indicate the presence of hydrogen aggregations in the polycrystalline interfacial SmNiO<sub>3</sub>, and the interfacial hydrogen concentration ( $n_{\text{H-Interf.}}$ ) increases with the duration of hydrogenation.

It should be noted that  $n_{\text{H-Interf.}}$  reaches a maximum magnitude of  $6.4 \times 10^{21} \text{ cm}^{-3}$  (H<sub>0.28</sub>SmNiO<sub>3</sub>), which is expected to be high enough to enable a percolated conduction path. This contrasts the hydrogen concentration measured at the quasi-single crystalline H<sub>x</sub>SmNiO<sub>3</sub> layer ( $n_{\text{H-Film}}$ ) that saturates at  $1.4 \times 10^{21} \text{ cm}^{-3}$  ( $x = 0.06$ ) at the shortest hydrogenation duration ( $t = 15$  min). The linear  $n_{\text{H-Interf.}}-t$  and saturating  $n_{\text{H-Film}}-t$  tendencies are more clearly demonstrated in Figure 3c. Concomitant with the elevation in  $n_{\text{H-Interf.}}$ , a reduced in-plane resistance of the sample is observed (see Figure S12 in the Supporting Information), while Figure 3d more clearly demonstrates the linear enhancement in the in-plane electrical conductance ( $S$ ) with  $n_{\text{H-Interf.}}$ . Considering the saturation of  $n_{\text{H-Film}}$  within their top SmNiO<sub>3</sub> film while their underneath LaAlO<sub>3</sub> is insulating, the  $S$ - $n_{\text{H-Interf.}}$  linearity is a clear experimental indication in support of our proposed more-heavily hydrogen doping effect enhanced electronic conductance from filling the upper Hubbard band (UHB) of the nickelate.

It is undeniable that the oxygen vacancy can be generated during the hydrogenation process that may also contribute to the transport behaviors. It is worthy to note that the electrical conductance for the co-lattice deposited SmNiO<sub>3</sub> on SrTiO<sub>3</sub> also shows a linear enhancement with the elongation of the hydrogen annealing period (see Figure S13a in the Supporting Information), while no incorporated hydrogen composition was detected via NRA (see Figure S13b in the Supporting Information). Nevertheless, the magnitude of the enhancement in the electrical conduction is more than one order smaller in magnitude as compared to the hydrogenated Pt/SmNiO<sub>3</sub>/LaAlO<sub>3</sub>, and therefore is more likely to be associated to the generation of oxygen vacancy. This understanding is supported by the smaller plateau frequency and larger activation energy in the AC-impedance spectrum observed in the hydrogenated Pt/SmNiO<sub>3</sub>/SrRuO<sub>3</sub>/SrTiO<sub>3</sub>, compared to Pt/SmNiO<sub>3</sub>/SrRuO<sub>3</sub>/LaAlO<sub>3</sub> and Pt/SmNiO<sub>3</sub>/SrRuO<sub>3</sub>/Si (see Figure S9 in the Supporting Information). Hence, grain boundary hydrogen doping for polycrystalline heterostructure should not be dominated by oxygen vacancy formation.

To further investigate the variation in the defect states when hydrogenating SmNiO<sub>3</sub>, we performed the positron annihilation spectroscopy (PAS) measurements for defective SmNiO<sub>3</sub>/LaAlO<sub>3</sub> and SmNiO<sub>3</sub>/SrTiO<sub>3</sub> before and after the hydrogenation process. As illustrated in Figure 3e, the <sup>22</sup>Na source was used to generate positron with continuously adjustable incident energies, while the penetration depth of the positron is calculated by  $R = (40\rho^{-1}) E^{1.6}$ , where  $R$  is the penetration depth (unit: nm),  $\rho$  is the density (unit: g cm<sup>-3</sup>), and  $E$  is the energy of positron (unit: keV). The positron annihilation generated  $\gamma$ -ray is detected in the form of Doppler broadening spectroscopy (DBS) from which the  $S$ -parameter (Shape) and  $W$ -parameter (Wing) are derived. The area of  $A$ ,  $B$ , and  $C$  represent for the number of collected  $\gamma$ -ray in the following three ranges of wavelength: 510.2–511.8, 505.1–508.4, and 513.6–516.9 keV, respectively, while  $\Delta$  represents for the total number of  $\gamma$ -ray collected from 499.5 to 522.5 keV. At each energy of the incident positron, the  $S$ -parameter associated to annihilation with low momentum electrons (e.g., localized electrons within defects) is derived by  $A/\Delta$ , while the  $W$ -parameter associated to annihilation with high momentum electrons (e.g., inner shell electrons) is derived by  $(B + C)/\Delta$ . Figure 3f shows the  $S$ - and

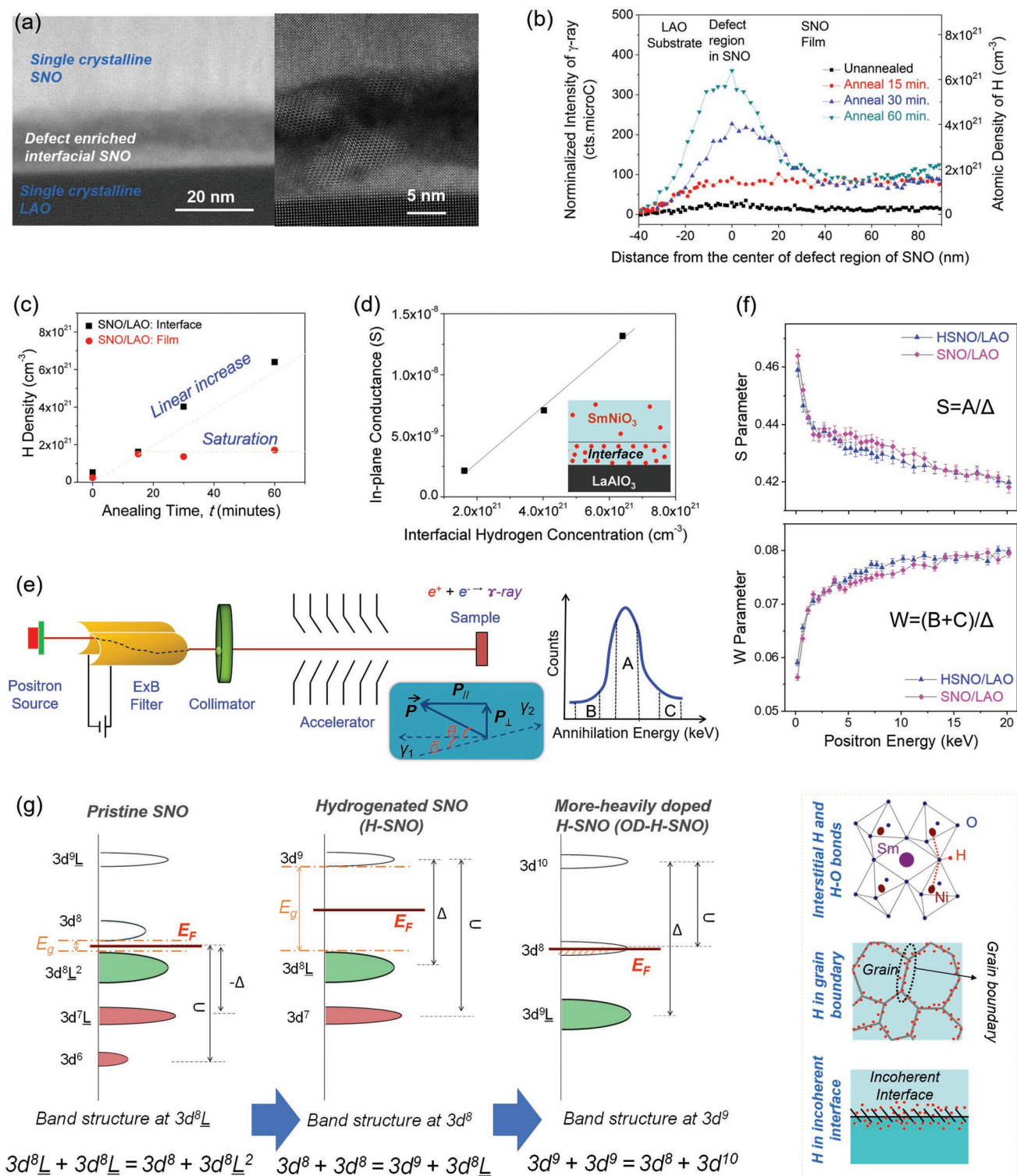


**Figure 3.** Quantitative relation of overdoping concentration and conductivity. a) TEM image of the  $\text{SmNiO}_3/\text{LaAlO}_3$  interface after cycles of thermoshock, demonstrating that an  $\sim 20$  nm wide interfacial region of  $\text{SmNiO}_3$  is broken into polycrystals that are sandwiched between the single crystalline  $\text{LaAlO}_3$  substrate and the top layer single crystalline  $\text{SmNiO}_3$ . b) NRA hydrogen profiles across the interfacial region of  $\text{SmNiO}_3/\text{LaAlO}_3$  after annealing in 1%  $\text{H}_2/\text{He}$  for various periods. c) Hydrogen concentration measured in the interfacial region of  $\text{SmNiO}_3/\text{LaAlO}_3$  and the top layer of the  $\text{SmNiO}_3$  film material plotted as a function of the hydrogenation periods. d) In-plane electrical conductance of  $\text{SmNiO}_3/\text{LaAlO}_3(001)$  plotted as a function of the interfacial hydrogen concentration. e) Working principle of the positron annihilation spectroscopy (PAS). f) The S- and W-parameter in PAS plotted as a function of the positron annihilation energy for  $\text{SmNiO}_3/\text{LaAlO}_3$  before and after the hydrogenation. g) Illustrating the hydrogen doping effect and related Mott transition via modifying the filling of Mott–Hubbard bands in nickelates, and more heavily hydrogen doping is expected when hydrogen accumulated at the defect regions.

$W$ -parameter from the PAS of  $\text{SmNiO}_3/\text{LaAlO}_3$  before and after the hydrogenation process, while their respective DBS are shown in Figures S14 and S15 in the Supporting Information, respectively. It can be seen that the incorporated hydrogen composition as indicated by Figure 3d reduces the  $S$ -parameter and enlarges the  $W$ -parameter in the incident energy range of positron corresponding to the penetration depth across the  $\text{SmNiO}_3$  film, while the parameters for the hydrogenated and pristine  $\text{Pt}/\text{SmNiO}_3/\text{LaAlO}_3$  are observed to be similar at either higher (corresponding to the substrate) or lower (corresponding to the Pt) energy range of the incident positron. These observations indicate that the incorporated hydrogen composition reduces the low momentum electrons associated to the lattice defect, similar to the hydrogen passivation of the defect states or dangling bonds for conventional semiconductors. In contrast, the hydrogenation of  $\text{SmNiO}_3/\text{SrTiO}_3$  (no hydrogen composition physically incorporated within  $\text{SmNiO}_3$ ) results in an enlarged  $S$ -parameter and reduced  $W$ -parameter (see Figure S16 in the Supporting Information), indicating the increase in lattice defects (e.g., oxygen vacancies) via the hydrogenation processes.

With the above results, we can conclude on the clear difference between the hydrogen anneal induced insulating transition and hydrogen composition doping of these  $\text{SmNiO}_3$ -based heterostructures. Although hydrogenation triggers the formation of the electron localized high-resist state of  $\text{SmNiO}_3$ , it does not require the practical incorporation of the hydrogen composition. As pointed out in previous literatures, the rare-earth nickelates exhibit abundant oxygen holes in the ground state,<sup>[1,12,16]</sup> and the hydrogenation process results in the formation of lattice defects, as clearly indicated by the PAS of  $\text{SmNiO}_3/\text{SrTiO}_3$  (see Figure S16 in the Supporting Information). The practical incorporation of the hydrogen composition is more associated to the hydrogen aggregation and passivation of the grain boundaries and interfacial defects within  $\text{SmNiO}_3$ , and this elevates the electrical conduction along the defective regions. It is also worth noticing that the proton conduction for oxides were reported to occur within grains,<sup>[26]</sup> grain boundaries,<sup>[27,28]</sup> and even along the surface,<sup>[29,30]</sup> while it also enriches the way to regulate the transportations associated to grain boundaries, i.e., via the tunneling regime.<sup>[31,32]</sup> Considering the herein observed much higher cross-plane conduction for hydrogenated polycrystalline  $\text{Pt}/\text{SmNiO}_3/\text{SrRuO}_3/\text{Si}$  compared to single crystalline  $\text{Pt}/\text{SmNiO}_3/\text{SrRuO}_3/\text{LaAlO}_3$  at their similar hydrogen concentration, the dominant proton conduction within  $\text{SmNiO}_3$  should be associated to the grain boundary.

Figure 3g illustrates the hydrogen-induced electron localization for  $\text{SmNiO}_3$  to result in the highly insulating state ( $t_{2g}^6 e_g^0 + t_{2g}^6 e_g^2$  to  $t_{2g}^6 e_g^2$ ), as well as the more heavily hydrogen doping within its defect region to produce a metallic phase ( $t_{2g}^6 e_g^2$  to  $t_{2g}^6 e_g^3$ ). It is noted that charge ordering does not need occur in an integer manner, while more details about the electronic structure are discussed in Section S4 in the Supporting Information. The Fermi level of the  $t_{2g}^6 e_g^3$  phase is expected to be further elevated into the Hubbard band by introducing additional carriers, resulting in electronic conductance. Such hydrogen doping effect should be considered as a rival effect compared with the reported hydrogenation-induced electron localization,<sup>[1–5]</sup> and will most likely occur in hydrogen aggregation regions such as grain boundaries and incoherent interfaces.

It should also be noted that in other nickelate compounds, nickel valence state reduction could be achieved from removing oxygen along with a significant change of the crystal structures,<sup>[33–35]</sup> which is not seen in our case. Further, we have found that when the rare-earth ion is large (for example,  $\text{LaNiO}_3$ ), it is very challenging to modify the conductivity of the materials via our hydrogen doping method,<sup>[3]</sup> which is not the case in other studies.<sup>[33–35]</sup> So these observations indicate that we should encounter different mechanisms, and why such discrepancy exists currently remains unknown. Possible reasons include the use of different conditions or different parent materials (e.g., bulk  $\text{ReNiO}_3$  vs Ruddlesden–Popper layered<sup>[35]</sup>). In addition, according to the recent discovery of superconductivity in reduced layered nickelate, such as  $\text{Nd}_{0.8}\text{Sr}_{0.2}\text{NiO}_2$ ,<sup>[36]</sup> a possible Sr–Sm intermixing in combination with oxygen vacancies at the interface between  $\text{SrRuO}_3$  and  $\text{SmNiO}_3$  may also influence electron configurations of the nickelate. Nevertheless, even intermixing of Sr and Sm exists to make the initial electronic structure carry a fraction of  $t_{2g}^6 e_g^0$ ,<sup>[36]</sup> the overall physics still holds since the majority part of the initial electronic configuration is  $t_{2g}^6 e_g^1$ . In a first order approximation, hybridization variance in different valence states of nickel ion<sup>[37,38]</sup> would not change the overall metal–insulator–metal phase transition process. Since we only observed the conductivity change after hydrogenation, so other processes may not contribute to the observed dynamic behavior.

In summary, we have discovered and demonstrated a high-concentration hydrogen doping effect within the defect region of rare-earth nickelates that overcompensate their conventional hydrogenation-induced electron localization. It further results in electric conductance in hydrogen-aggregated regions such as grains boundaries and incoherent interfaces via partially filling the Hubbard band of  $\text{H}_x\text{SmNiO}_3$ . By harnessing this understanding, we have demonstrated a novel Mottronic nickelate device in hydrogenated  $\text{Pt}/\text{H}_x\text{SmNiO}_3/\text{SrRuO}_3$  heterostructures. From the fundamental aspect, the correlation between the hydrogen doping concentration and the resulting conductance increase has been unveiled through NRA, PAS, and electronic transport studies. Introducing a high-concentration hydrogen doping via interfacial engineering and/or grain boundary designs in electron-correlated perovskite materials opens new avenues to explore novel iontronic devices for emerging computing and memory technologies.

## Experimental Section

**Sample Preparation:** Thin films of  $\text{SmNiO}_3$ ,  $\text{NdNiO}_3$ , and  $\text{EuNiO}_3$  were grown on  $\text{SrRuO}_3(001)$  buffered substrates, such as quartz ( $\text{SiO}_2$ ), single crystalline Si (001), single crystalline  $\text{SrTiO}_3(001)$ , and single crystalline  $\text{LaAlO}_3(001)$ , by pulsed laser deposition. The ceramic target with nominal composition of  $\text{SmNiO}_3$ ,  $\text{NdNiO}_3$ , and  $\text{EuNiO}_3$  was ablated by a 248 nm laser beam inside a vacuum chamber at an  $\text{O}_2$  background pressure of  $\approx 20$  Pa, while the temperature of the substrates was kept constant at  $\approx 650$  °C. To hydrogenate as-grown thin films, Pt electrodes were deposited by laser ablation of a Pt metal target at 1 Pa Ar pressure with a substrate temperature of  $\approx 20$  °C. The hydrogenation was performed by annealing the sample in a 1%  $\text{H}_2/\text{He}$  gas mixture with an atmosphere pressure at 300 °C for various periods from 15 to 120 min, while dehydrogenation was performed by annealing the sample in  $\text{O}_2$  gas at 300 °C for 30 min.

**Characterizations:** The crystal structures were characterized by XRD for polycrystalline thin films, such as  $\text{SmNiO}_3/\text{SrRuO}_3/\text{Si}$ ,  $\text{SmNiO}_3/\text{SrRuO}_3/\text{SiO}_2$ ,  $\text{NdNiO}_3/\text{SrRuO}_3/\text{Si}$ ,  $\text{NdNiO}_3/\text{SrRuO}_3/\text{SiO}_2$ ,  $\text{EuNiO}_3/\text{SrRuO}_3/\text{Si}$ , and  $\text{EuNiO}_3/\text{SrRuO}_3/\text{SiO}_2$ . To avoid the diffractions from the substrate, the X-ray was flipped over the surface of the thin film at a small incident angle (i.e.,  $0.5^\circ$ ). The cross-section structures of as-grown films were characterized by high-angle annular dark-field (HAADF) and annular bright-field (ABF) scanning transmission electron microscopy (STEM) performed on JEM-ARM 200F TEM operated at 200 kV with a cold field emission gun and aberration correctors for both probe-forming and imaging lenses. The hydrogen depth profiles within the thin films were characterized by NRA in the Micro Analysis Laboratory, Tandem accelerator (MALT) at The University of Tokyo. The PAS was performed at multidiscipline research center, Institute of High Energy Physics, CAS, Beijing. More details about the working principle and curve fitting for NRA and PAS experiments are given in the Supporting Information.

## Supporting Information

Supporting Information is available from the Wiley Online Library or from the author.

## Acknowledgements

J.C. and W.M. contributed equally to this work. This work was supported by the National Natural Science Foundation of China (Nos. 51602022 and 61674013). J.C. also appreciates the Japanese Society for the Promotion of Science (Fellowship ID: P15363). Y.J. also acknowledges National Natural Science Foundation of China, Key Program (No.51731003). L.G. was supported by the National Key Research and Development Program of China (Grant No. 2017YFB0702100). Z.C. and J.S. were supported by the National Science Foundation under Award #1706815 and the Air Force Office of Scientific Research under award number FA9550-18-1-0116. J.S. was also supported by the NYSTAR Focus Center at Rensselaer Polytechnic Institute (RPI) under award No. C150117. The authors appreciate helpful discussions and technical supports by Prof. Akira Toriumi, Prof. Katsuyuki Fukutani, and Prof. Hiroyuki Matsuzaki from The University of Tokyo (Japan); and Prof. Lidong Chen from Shanghai Institute of Ceramics, Chinese Academy of Sciences (China).

## Conflict of Interest

The authors declare no conflict of interest.

## Keywords

electron correlation, electronic phase transitions, hydrogen doping, perovskite oxides, rare-earth nickelates

Received: August 5, 2019

Revised: November 21, 2019

Published online: December 19, 2019

- [1] J. Shi, Y. Zhou, S. Ramanathan, *Nat. Commun.* **2014**, *5*, 4860.  
[2] F. Zuo, P. Panda, M. Kotiuga, J. Li, M. Kang, C. Mazzoli, H. Zhou, A. Barbour, S. Wilkins, B. Narayanan, M. Cherukara, Z. Zhang, S. K. R. S. Sankaranarayanan, R. Comin, K. M. Rabe, K. Roy, S. Ramanathan, *Nat. Commun.* **2017**, *8*, 240.

- [3] J. Chen, Y. Zhou, S. Middey, J. Jiang, N. Chen, L. Chen, X. Shi, M. Döbeli, J. Shi, J. Chakhalian, S. Ramanathan, *Appl. Phys. Lett.* **2015**, *107*, 031905.  
[4] Z. Zhang, D. Schwanz, B. Narayanan, M. Kotiuga, J. A. Dura, M. Cherukara, H. Zhou, J. W. Freeland, J. Li, R. Sutarto, F. He, C. Wu, J. Zhu, Y. Sun, K. Ramadoss, S. S. Nonnenmann, N. Yu, R. Comin, K. M. Rabe, S. K. R. S. Sankaranarayanan, S. Ramanathan, *Nature* **2018**, *553*, 68.  
[5] Y. Zhou, X. F. Guan, H. Zhou, K. Ramadoss, S. Adam, H. J. Liu, S. Lee, J. Shi, M. Tsuchiya, D. D. Fong, S. Ramanathan, *Nature* **2016**, *534*, 231.  
[6] N. P. Lu, P. F. Zhang, Q. H. Zhang, R. M. Qiao, Q. He, H. B. Li, Y. J. Wang, J. W. Guo, D. Zhang, Z. Duan, Z. L. Li, M. Wang, S. Z. Yang, M. Z. Yan, E. Arenholz, S. Y. Zhou, W. L. Yang, L. Gu, C. W. Nan, J. Wu, Y. Tokura, P. Yu, *Nature* **2017**, *546*, 124.  
[7] H. Yoon, M. Choi, T.-W. Lim, H. Kwon, K. Ihm, J. K. Kim, S.-Y. Choi, J. Son, *Nat. Mater.* **2016**, *15*, 1113.  
[8] K. Vanheusden, W. L. Warren, R. A. B. Devine, D. M. Fleetwood, J. R. Schwank, M. R. Shaneyfelt, P. S. Winokur, Z. J. Lemnios, *Nature* **1997**, *386*, 587.  
[9] H. Yuan, H. Shimotani, A. Tsukazaki, A. Ohtomo, M. Kawasaki, Y. Iwasa, *J. Am. Chem. Soc.* **2010**, *132*, 6672.  
[10] J. Yoon, W. K. Hong, M. Jo, G. Jo, M. Choe, W. Park, J. I. Sohn, S. Nedic, H. Hwang, M. E. Welland, T. Lee, *ACS Nano* **2011**, *5*, 558.  
[11] V. Bisogni, S. Catalano, R. J. Green, M. Gibert, R. Scherwitzl, Y. Huang, V. N. Strocov, P. Zubko, S. Balandeh, J. M. Triscone, G. Sawatzky, T. Schmitt, *Nat. Commun.* **2016**, *7*, 13017.  
[12] J. Varignon, M. N. Grisolia, J. Iñiguez, A. Barthélémy, *npj Quantum Mater.* **2017**, *2*, 21.  
[13] R. Jaramillo, F. Schoofs, S. D. Ha, S. Ramanathan, *J. Mater. Chem. C* **2013**, *1*, 2455.  
[14] R. Jaramillo, S. D. Ha, D. M. Silevitch, S. Ramanathan, *Nat. Phys.* **2014**, *10*, 304.  
[15] J. Shi, S. D. Ha, Y. Zhou, F. Schoofs, S. Ramanathan, *Nat. Commun.* **2013**, *4*, 2676.  
[16] G. Catalan, *Phase Transitions* **2008**, *81*, 729.  
[17] F. Y. Bruno, K. Z. Rushchanskii, S. Valencia, Y. Dumont, C. Carrétéro, E. Jacquet, R. Abrudan, S. Blügel, M. Ležaić, M. Bibes, A. Barthélémy, *Phys. Rev. B* **2013**, *88*, 195108.  
[18] N. Shukla, T. Joshi, S. Dasgupta, P. Borisov, D. Lederman, S. Datta, *Appl. Phys. Lett.* **2014**, *105*, 012108.  
[19] F. Conchon, A. Boule, R. Guinebrière, C. Girardot, S. Pignard, J. Kreisel, F. Weiss, E. Dooryhée, J. L. Hodeau, *Appl. Phys. Lett.* **2007**, *91*, 192110.  
[20] M. Wilde, K. Fukutani, *Surf. Sci. Rep.* **2014**, *69*, 196.  
[21] T. K. Gupta, *J. Am. Ceram. Soc.* **1990**, *73*, 1817.  
[22] R. Einzinger, *Annu. Rev. Mater. Sci.* **1987**, *17*, 299.  
[23] S. Lambardo, A. L. Magna, C. Gerardi, M. Alessandri, F. Crupi, *Appl. Phys. Lett.* **1999**, *75*, 1161.  
[24] E. Miranda, J. Suñé, R. Rodríguez, M. Nafria, X. Aymerich, *Appl. Phys. Lett.* **1998**, *73*, 490.  
[25] M. Houssa, T. Nigam, P. W. Mertens, M. M. Heyns, *Appl. Phys. Lett.* **1998**, *73*, 514.  
[26] Y. J. Kao, C. Y. Su, C. Pithan, D. F. Hennings, C. Y. Huang, R. Waser, *J. Am. Ceram. Soc.* **2016**, *99*, 1311.  
[27] K. Thabet, M. Devisse, E. Quarez, O. Joubert, A. L. G. L. Salle, *Solid State Ionics* **2018**, *325*, 48.  
[28] A. K. Baral, *Solid State Ionics* **2015**, *272*, 107.  
[29] S. O. Stub, E. Vollestad, T. Norby, *J. Mater. Chem. A* **2018**, *6*, 8265.  
[30] C. Tandé, D. Pérez-Coll, G. C. Mather, *J. Mater. Chem.* **2012**, *22*, 11208.  
[31] R. Gross, L. Alff, B. Büchner, B. H. Freitag, C. Höfener, J. Klein, Y. Lu, W. Mader, J. B. Philipp, M. S. R. Rao, P. Reutler, S. Ritter,

- S. Thienhaus, S. Uhlenbruck, B. Wiedenhorst, *J. Magn. Magn. Mater.* **2000**, 211, 150.
- [32] I. Fina, G. Apachitei, D. Preziosi, H. Deniz, D. Kriegner, X. Marti, M. Alexe, *Sci. Rep.* **2015**, 5, 14367.
- [33] M. Crespin, P. Levitz, L. Gatineau, *J. Chem. Soc., Faraday Trans. 2* **1983**, 79, 1181.
- [34] P. Levitz, M. Crespin, L. Gatineau, *J. Chem. Soc., Faraday Trans. 2* **1983**, 79, 1195.
- [35] J. Zhang, A. S. Botana, J. W. Freeland, D. Phelan, H. Zheng, V. Pardo, M. R. Norman, J. F. Mitchell, *Nat. Phys.* **2017**, 13, 864.
- [36] D. Li, K. Lee, B. Y. Wang, M. Osada, S. Crossley, H. R. Lee, Y. Cui, Y. Hikita, H. Y. Hwang, *Nature* **2019**, 572, 624.
- [37] M. Jiang, M. Berciu, G. A. Sawatzky, arXiv:1909.02557 **2019**.
- [38] M. Hepting, D. Li, C. J. Jia, H. Lu, E. Paris, Y. Tseng, X. Feng, M. Osada, E. Been, Y. Hikita, Y. D. Chuang, Z. Hussain, K. J. Zhou, arXiv:1909.02678 **2019**.